Ambient seismic noise monitoring of a clay landslide: Toward failure prediction.

Guénolé Mainsant, Éric Larose, Cornelia Brönnimann, Denis Jongmans, Clément Michoud, Michel Jaboyedoff

Ambient seismic noise monitoring of a clay landslide: Toward failure prediction

Guénolé Mainsant,[1] Eric Larose,[1] Cornelia Brönnimann,[2] Denis Jongmans,[1] Clément Michoud,[3] and Michel Jaboyedoff[3]

Received 29 July 2011; revised 1 February 2012; accepted 6 February 2012; published 22 March 2012.

[1] Given that clay-rich landslides may become mobilized, leading to rapid mass movements (earthflows and debris flows), they pose critical problems in risk management worldwide. The most widely proposed mechanism leading to such flow-like movements is the increase in water pore pressure in the sliding mass, generating partial or complete liquefaction. This solid-to-liquid transition results in a dramatic reduction of mechanical rigidity in the liquefied zones, which could be detected by monitoring shear wave velocity variations. With this purpose in mind, the ambient seismic noise correlation technique has been applied to measure the variation in the seismic surface wave velocity in the Pont Bourquin landslide (Swiss Alps). This small but active composite earthslide-earthflow was equipped with continuously recording seismic sensors during spring and summer 2010. An earthslide of a few thousand cubic meters was triggered in mid-August 2010, after a rainy period. This article shows that the seismic velocity of the sliding material, measured from daily noise correlograms, decreased continuously and rapidly for several days prior to the catastrophic event. From a spectral analysis of the velocity decrease, it was possible to determine the location of the change at the base of the sliding layer. These results demonstrate that ambient seismic noise can be used to detect rigidity variations before failure and could potentially be used to predict landslides.

Citation: Mainsant, G., E. Larose, C. Brönnimann, D. Jongmans, C. Michoud, and M. Jaboyedoff (2012), Ambient seismic noise monitoring of a clay landslide: Toward failure prediction, *J. Geophys. Res.*, *117*, F01030, doi:10.1029/2011JF002159.

1. Introduction

[2] All mountainous areas are affected by gravitational mass movements of various types, sizes and velocities, which could have a major impact on life and property. Landslides in clay-rich formations, which are widespread over the world, are characterized by unpredictable acceleration and liquefaction phases [*Iverson et al.*, 1997*; Malet et al.*, 2005]. Of particular concern for hazard assessment is the triggering of earthflows and debris flows, the rheology of which switches from solid to fluid. This phenomenon has been widely reported in all types of recent clay deposits, including Quaternary marine sensitive [*Crawford*, 1968; *Eilertsen et al.*, 2008] or nonsensitive clays [*Picarelli et al.*, 2005] and lacustrine clay deposits [*Bièvre et al.*, 2011]. But flow-like movements have also been frequently observed in fractured and weathered clay-rich rocks, such as shales, marls and flyschs [*Angeli et al.*, 2000; *Picarelli et al.*, 2005; *Malet et al.*, 2005], and in volcanic rocks in which primary minerals were altered to clays [*Coe et al.*, 2003].

[3] Predicting these sudden events, primarily controlled by groundwater conditions, has been an active research topic for the last two decades [*Lee and Ho*, 2009]. Empirical prediction methods have been proposed, relying on two types of measurements: (1) surface displacements, whose change to rupture is usually interpreted using slope creep theories [*Petley et al.*, 2005], and (2) hydrological factors such as precipitation, soil water content or pore pressure, used as predictors with threshold values determined in an empirical or statistical manner [*Keefer et al.*, 1987]. Although these empirical methods have been successfully applied in some specific cases, they do not provide a real insight into the mechanisms involved, and have proved to be very sensitive to changes in landslide geometry and deformation. Recently, theoretical models coupling a slope instability mechanism and hydrological modeling have been developed for predicting landslide occurrence [*Keefer et al.*, 1987*; Crosta and Frattini*, 2008]. However, in 3D, such approaches require considerable investigation and computational effort.

[4] For debris flows and earthflows occurring in fine-grained soils during or after heavy and sustained rainfalls, the triggering mechanism most often proposed is the partial or total liquefaction of the mass, resulting from an increase in pore water pressure [*Picarelli et al.*, 2005; *van Asch et al.*, 2007]. As the shear wave velocity (V_s) in a fluid tends to 0 [*Reynolds*, 1997], the bulk shear wave velocity should

[1]ISTerre, CNRS, Université de Grenoble, Grenoble, France.
[2]GEOLEP, EPFL, Lausanne, Switzerland.
[3]IGAR, University of Lausanne, Lausanne, Switzerland.

0148-0227/12/2011JF002159

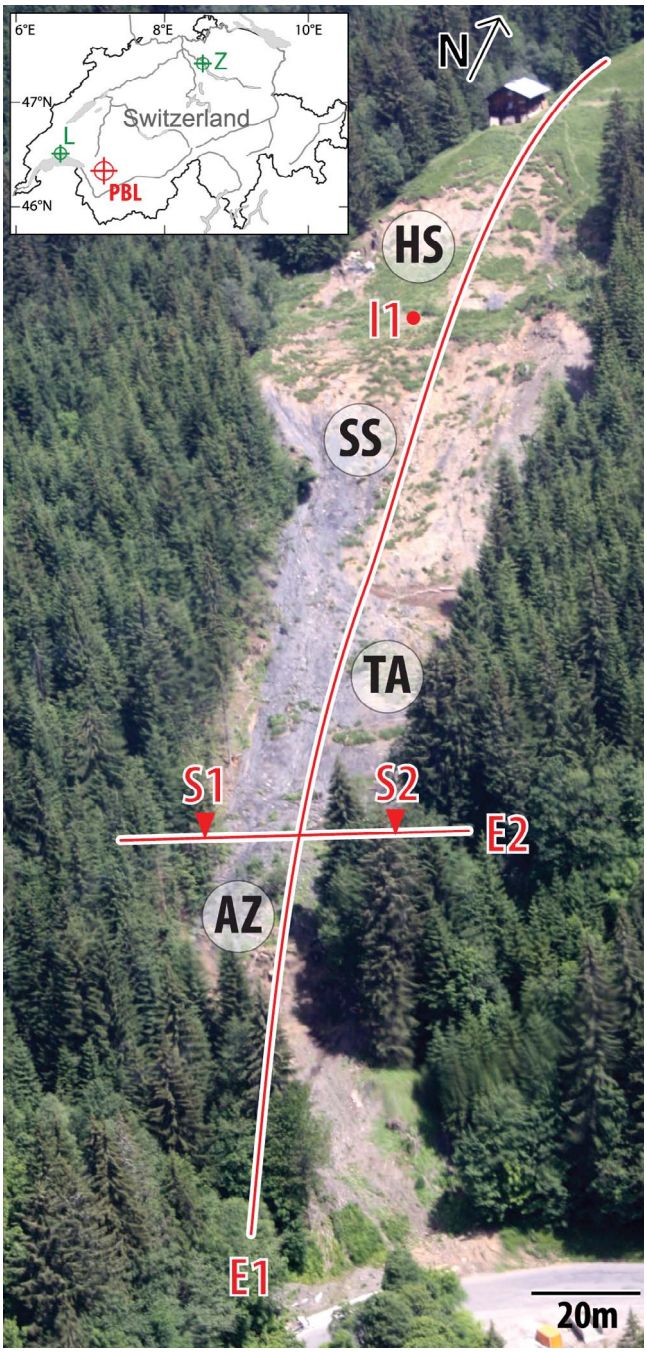

Figure 1. Aerial photo of the Pont Bourquin landslide in June 2009, with the location of the two electrical profiles E1 and E2, the two seismometers S1 and S2 installed on stable ground, and the inclinometer I1. The headscarp (HS), main secondary scarp (SS), transportation area (TA), and accumulation zone (AZ) are also indicated. The Pont Bourquin landslide (red cross) is located on the topographic inset map of Switzerland (L, Lausanne; Z, Zurich). The gravitational instability threatens the road carrying heavy traffic over the Pillon pass (bottom of the photo).

dramatically decrease in the vicinity of liquefied zones. Moreover, it has been recently shown that, in a clay-rich landslide, V_s also significantly decreases with the extent of damage in the material [*Renalier et al.*, 2010]. This suggests that continuous V_s measurement could be valuable for monitoring clay slope degradation and would constitute an alternative to the classical prediction methods. V_s is usually obtained from active source-receiver experiments. However, the reproducibility of seismic sources is very limited, and it is difficult to ascertain whether seismic response changes actually result from a change in the mechanical properties of the medium or from the source. The ambient noise correlation technique developed over the last 10 years [*Weaver and Lobkis*, 2001*; Shapiro and Campillo*, 2004] offers a realistic alternative to using controlled sources. The local Green's function (or impulse response) can in fact be determined from the cross correlation of ambient noise continuously acquired by two passive sensors as if one of them was a source. This method has found considerable applications in seismic imaging at different scales [*Shapiro et al.*, 2005*; Larose et al.*, 2006]. More recently, it was demonstrated that the tail portion of the correlograms, the so-called coda part formed by scattered waves, is extremely sensitive to small changes in the medium [*Sens-Schönfelder and Wegler*, 2006*; Brenguier et al.*, 2008a, 2008b]. By comparing the phases of the waves in the coda, apparent relative velocity changes of the material can be measured with a precision better than 0.1%. This can be performed even if the correlograms do not give the exact Green's function between the sensors. Correlograms are however required to be stable in time, implying a relatively constant background noise over the period of interest [*Hadziioannou et al.*, 2009]. In the present manuscript we will apply the noise correlation technique on a landslide where the noise is in part due to traffic on the road, which constitutes a spatially stable background noise. The purpose of the paper is to detect mechanical changes in an active clay landslide where failure is expected.

2. The Pont Bourquin Landslide History and Geology

2.1. Historical Context

[5] The Pont Bourquin landslide is located in the Swiss Prealps, 40 km to the east of the town of Lausanne (Figure 1). Although the whole area has been affected by landslide phenomena since the last glacial retreat (more than 10,000 years ago), aerial photos show that gravitational deformation appeared in the mid 90s in the upper part of the hillside and that the slope instability gradually developed over a period of about 10 years [*Jaboyedoff et al.*, 2009]. In 2006, displacements of up to 80 cm created the head scarp of a 240 m long translational landslide affecting an area of about 8,000 m^2, with a width varying from 15 m to 60 m (Figure 1). On 5 July 2007, a 3 day period of heavy rainfall (cumulative depth of 95 mm) triggered an earthflow, which started from the main secondary scarp (SS in Figures 1 and 2) and cut the frequently used Pillon Pass road located at the toe of the Pont Bourquin landslide. This earthflow, with an estimated volume of 3,000 to 6,000 m^3, affected a layer a few meters thick in the transportation area (TA) of the Pont Bourquin landslide [*Jaboyedoff et al.*, 2009]. During the following 3 years, the entire landslide has exhibited a general translational motion associated with high internal deformation and numerous small superficial translational or rotational landslides, earthflows and debris flows. These

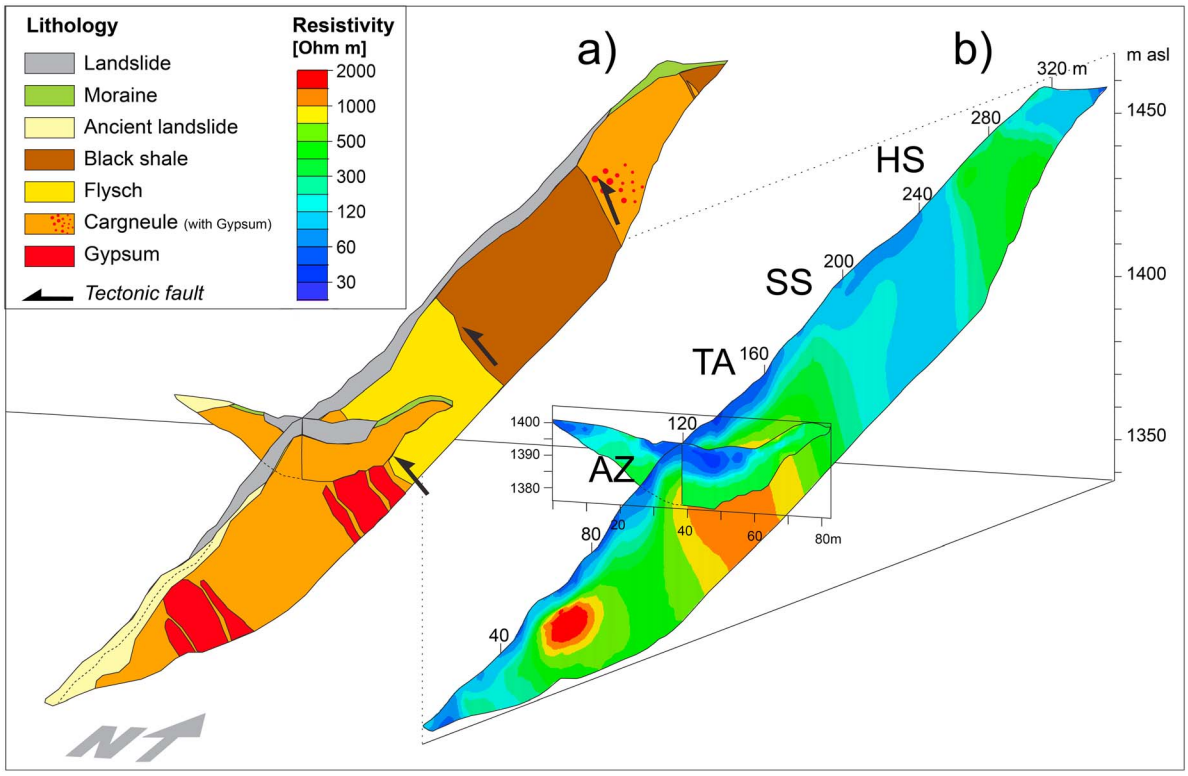

Figure 2. (a) North-south geological cross section along the Pont Bourquin landslide, constructed from the local geological atlas [*Badoux et al.*, 1990] and the electrical images shown in Figure 2b. (b) North-south and east-west oriented electrical resistivity tomography profiles (see location in Figure 1). The head-scarp (HS), main secondary scarp (SS), transportation area (TA), and accumulation zone (AZ) are also indicated.

multiple erosive processes gradually created a bulge of highly deformed material (accumulation zone labeled AZ in Figures 1 and 2) that progressively loaded the lower part of slope (see also Text S1 in the auxiliary material).[1] This material accumulation led to the toe failure between 18 and 20 August 2010, following significant cumulative rainfall in July.

2.2. Geological Context

[6] According to the geological map [*Badoux et al.*, 1990] the Pont Bourquin landslide is located in a tectonically very complex zone. Three thrust faults dipping approximately 35° toward the North cross the landslide and separate distinctive geological formations (Figure 2a). In the upper and lower parts of the slope, the bedrock is composed of Triassic cargneule (cellular dolomite) associated with gypsum. These highly soluble and deformable rocks could have promoted slope destabilization at the landslide toe. Below the cargneule layer, the upper part of the slope is made of Aalenian black shale, the weathering of which is the main source of the sliding clay material. In the middle part of the slope, the landslide overlies flysch consisting of thin-bedded turbidites including siltstone and conglomerate. The top of the hill is covered by several meters of moraine deposits. The rocks have been heavily fractured by the Alpine orogeny and subsequently affected by toppling, chemical weathering and freeze and thaw cycles, which contributed to a high degree of fragmentation of the outcropping rocks. These alterations have resulted in muddy material that can give rise to numerous small earthflows and debris flows along the slope. Deposits resulting from ancient mass movements locally cover the lower part of the slope. The present day landslide mass is mainly composed of a mixture of moraine material, mainly visible in the upper part, and weathered debris from the Aalenian black shale, flysch sandstone and marl alternations, making the sliding material predominantly clayey. According to the classification proposed by *Cruden and Varnes* [1996], this landslide can be termed an active composite earthslide-earthflow.

2.3. Geophysical Investigation

[7] In order to clarify the landslide geometry and the geological structure underneath, two electrical resistivity tomography (ERT) profiles E1 and E2 were collected (see location in Figure 1), along and perpendicular to the slope, respectively. Data were acquired using the Wenner-Schlumberger configuration [*Dahlin and Zhou*, 2004] with 64 electrodes and an electrode spacing of 5 m and 1.5 m for E1 and E2, respectively. Data were inverted through a least squares inversion (L2-norm) using the RES2DINV software [*Loke*, 1998]. ERT images have been obtained for a RMS value lower than 5%. Electrical images are shown in Figure 2b. The superficial clay-rich sliding layer is clearly

[1]Auxiliary materials are available in the HTML. doi:10.1029/2011JF002159.

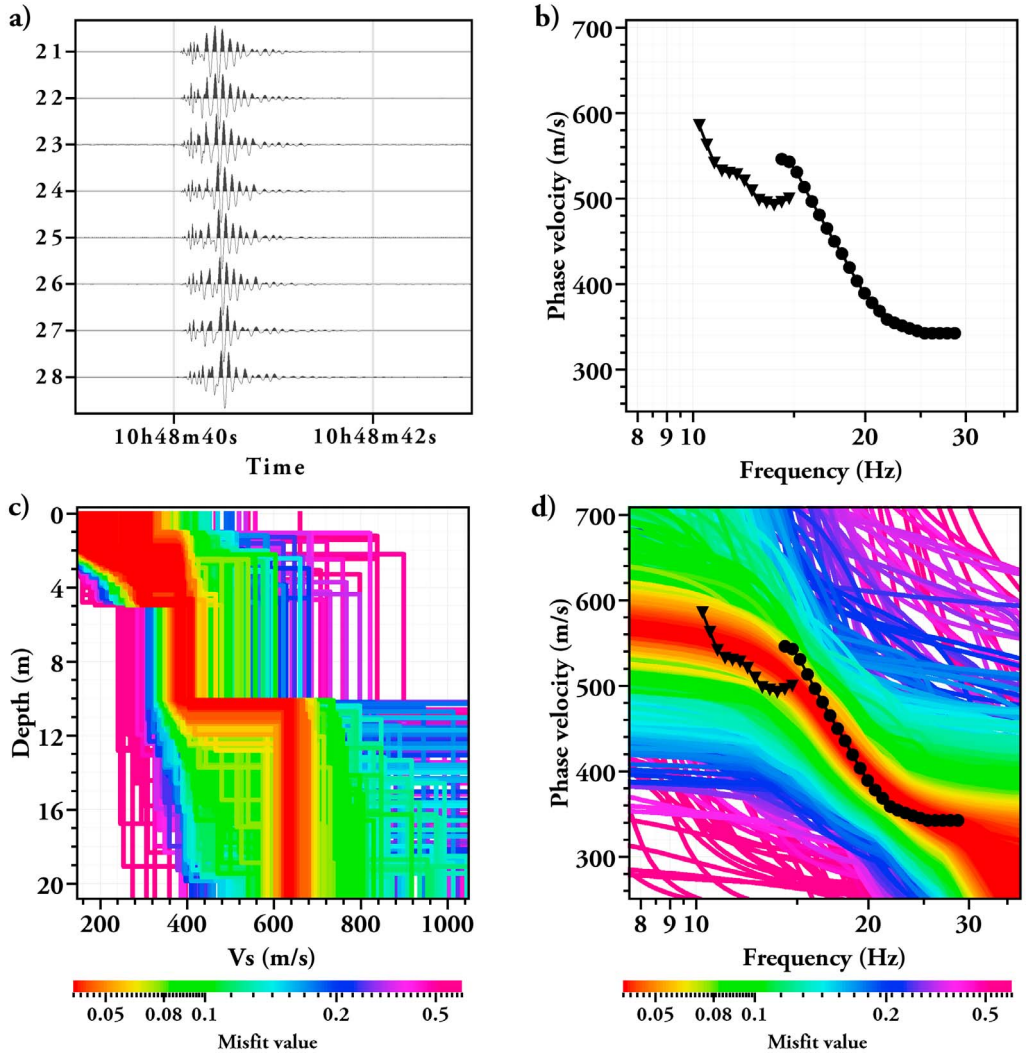

Figure 3. Shear wave velocity determination from the Rayleigh waves measured along two perpendicular profiles (same location as E1 and E2, Figure 1). (a) Normalized raw signals along profile 1. The spacing between geophones is 5 m. (b) Phase velocity dispersion curves computed from profiles 1 (triangles) and 2 (circles). (c) V_s profiles resulting from the inversion of dispersion curves with a three-layer model. (d) Dispersion curves corresponding to the models shown in Figure 3c.

evidenced by a resistivity lower than 100 ohm m, with a thickness varying from a few meters to locally more than 10 m along the profile. This low resistivity results from the high percentage of saturated clay in the sliding mass and from the high salinity of the water (total salinity greater than 1500 mg/l in superficial water between S1 and S2, Figure 1). The potentially mobilized volume of the whole landslide is estimated to be 30,000 to 40,000 m^3. Below the sliding material, the cargneule and gypsum formations at the top and bottom of the slope can be distinguished by their higher resistivity (from 200 to 500 ohm m in the cargneule and up to 2000 ohm m in gypsum). Conversely, the black shales are characterized by low resistivity values ranging from 100 to 200 ohm m. Finally, the flysch formation has a resistivity between 200 and 500 ohm m, a range similar to that measured for the cargneule. The combination of the two electrical images and geological observations has yielded the interpretative cross section of Figure 2a.

[8] Two active seismic profiles were performed along and across the landside (same location as the electrical profiles E1 and E2). The surface wave inversion technique was applied to 8 signals recorded in the accumulation zone of the landslide to infer the shear wave velocity profile in this area. For the longitudinal profile, signals were generated with explosive shots and recorded by 8 geophones 5 m apart (channels 21 to 28, Figure 3a). For the second transverse profile (between S1 and S2), the source was a hammer striking a plate, and the records from 8 geophones located within the landslide (4 m intertrace distance) were processed. The Rayleigh wave phase velocity dispersion curves were computed along the two perpendicular travel paths (Figure 3b), using the frequency-wave number technique [*Lacoss et al.*, 1969]. The two dispersion curves cover the 10–30 Hz frequency range, according to the frequency of the sources (explosive and hammer), and partly overlap around 15 Hz. The 10% difference in phase velocity around 15 Hz

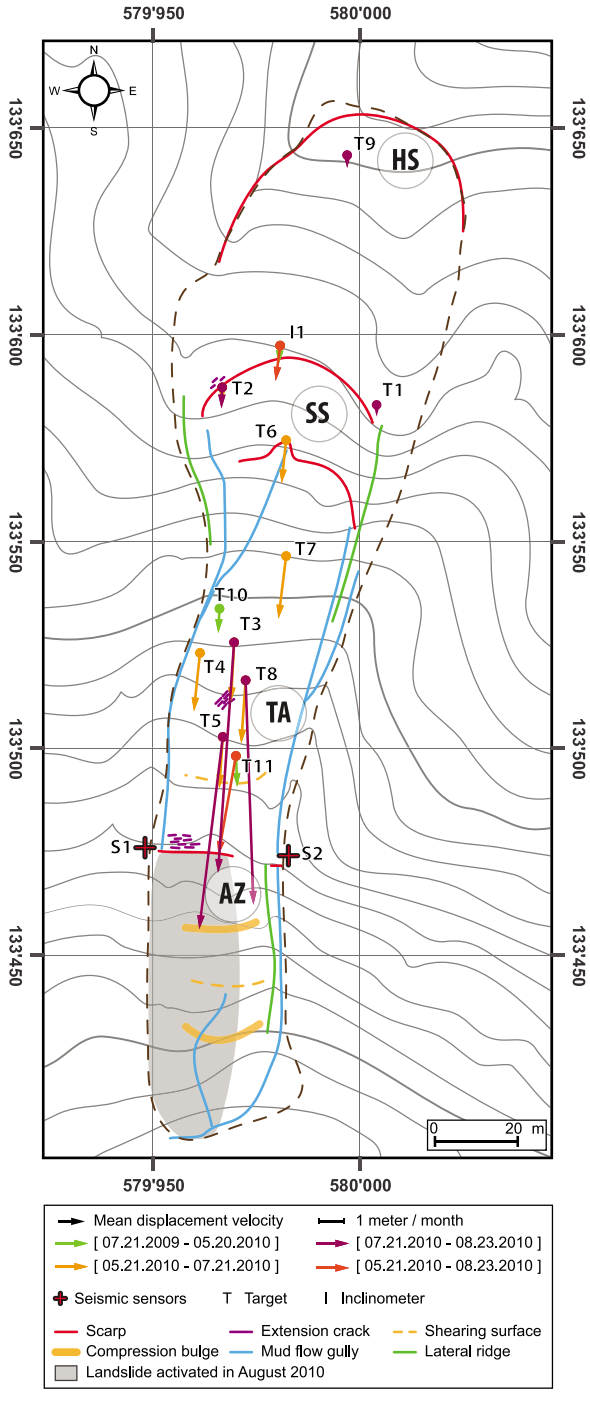

Figure 4. Mean velocity (meters per month) of 12 targets (T1–T11 and I1), monitored since July 2009 by Differential Global Navigation Satellite System (D-GNSS) and May 2010 by Electronic Distance Meter (EDM). In the top part of the landslide, displacements did not exceed 1 m between 20 May 2010 and 23 August 2010, while they exceeded 20 m in the middle of the transportation area during these 3 months, which considerably loaded the accumulation zone (AZ). (Topography outside the landslide: high-resolution Digital Elevation Model data from Swisstopo; topography inside the landslide: terrestrial laser scanning (TLS) data from UNIL.)

(500 to 550 m/s) probably results from different spatial variations along the two profiles. Dispersion curves were inverted using the enhanced neighborhood algorithm [*Wathelet*, 2008], assuming a 1D structure along the two directions below the accumulation zone. The misfit function is defined by the following equation:

$$misf = \sqrt{\frac{1}{n}\sum_{i=1}^{n}\frac{(c_{di}-c_{ci})^2}{{c_{di}}^2}}, \quad (1)$$

where c_{di} is the phase velocity of the data curve at frequency f_i, c_{ci} is the velocity of the calculated curve at frequency f, and n is the number of frequency samples. The inversion was constrained by imposing a thickness higher than 10 m for the clay-rich sliding layer, in agreement with the electrical data.

[9] Figure 3c shows the computed S wave velocity profiles with the misfit values for a three-layer model. The shear wave velocity in the superficial layer of a few meters thick is poorly constrained, owing to the lack of information at high frequency. Below, the best fitting models (misfit lower than 5%) show that the seismic velocity in the landslide is between 360 and 420 m/s. The bottom of this layer is found at a depth of about 11 m. Below this depth, the velocity increased to about 640 m/s in the undisturbed layers. Figure 3d displays all dispersion curves corresponding to the models obtained, with good agreement being shown between models and observations.

2.4. Groundwater Level Monitoring

[10] The level of the water table was measured in one 5 m deep borehole located in the accumulation zone (see Figure 4 for location). The system consists of a piezometer sensor connected to a data logger operated continuously, and a barometer to correct the water table height from the atmospheric pressure fluctuations. During the experiment time (April to August 2010), the measured water table fluctuated from 3.7 m depth to less than 1 m (see section 4.1).

3. Displacement Monitoring

3.1. Surface Displacement From GNSS and Electronic Distance Meter

[11] In order to evaluate the activity of the Pont Bourquin landslide, the displacement of twelve targets placed on the surface was recorded. Three targets (I1, T10 and T11, see location in Figures 1 and 4), were monitored from summer 2009 until August 2010 using a Differential Global Navigation Satellite System (D-GNSS) [*U.S. Army Corps of Engineers*, 2003]. The data were acquired by two Topcon HiPer® Pro antennas tracking their position from the Russian and American geodesic satellite constellations. The field procedure followed the Real Time Kinematic (RTK) method. A base station antenna was set up on a unique reference point location close to the landslide (about 650 m away). Targets on the landslide were 3D located with the second GNSS antenna (rover station), using the correction information communicated by the base station. Instrumental accuracy is ~12 mm [*Gili et al.*, 2000], which is considered negligible with regards to the observed meter-scale displacements. Nine additional targets (T1–T9) were installed

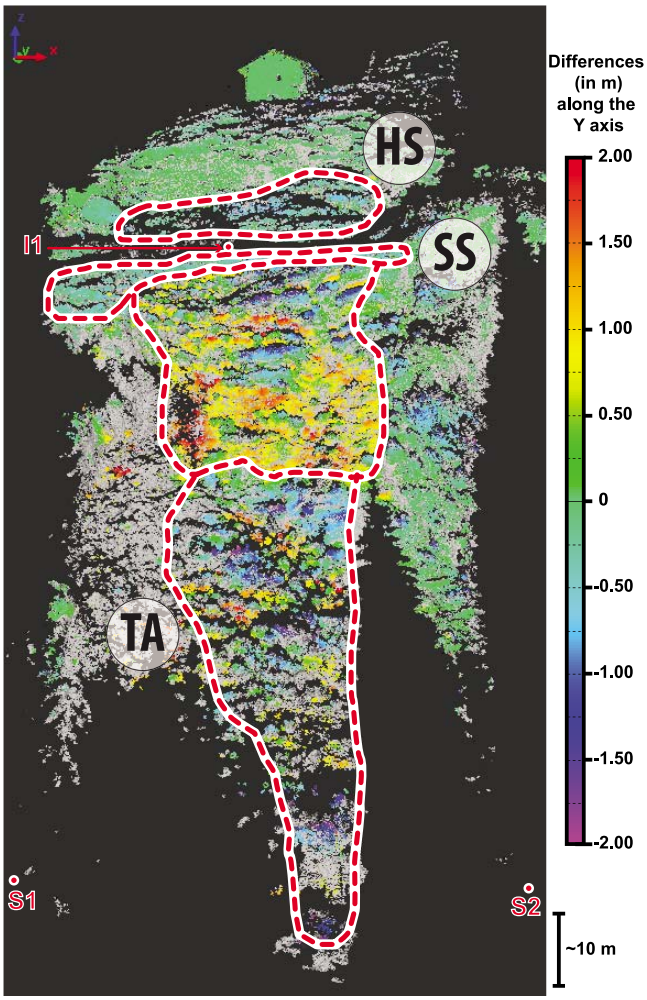

Figure 5. Differences (in m, southward, i.e., along the *y* axis) between two point clouds acquired by TLS on 19 May 2010 and on 20 July 2010. Positive (accumulated material) and negative (eroded material) movements are shown in red and blue, respectively. Black indicates no data, and gray indicates unreliable data. Red dashed lines isolate particular areas of the landslide. Small erosion of the head scarp (HS) by flowing processes. Retrogression of the most active secondary scarp (SS) through small and discontinuous translational landslides. Very active creeping inside the transportation area (TA). The locations of the inclinometer (I1) and the seismometers (S1 and S2) are indicated. The accumulation zone located between S1 and S2 could not be monitored by TLS because of forest cover.

in spring 2010 and have been periodically monitored with a Topcon GPT-9003M reflector total station [*U.S. Army Corps of Engineers*, 2007]. For each measurement campaign, the device was first installed at a reference point (the same as the GNSS base station) having a direct line of sight to the landslide and orientated by shooting at a reference prism located in a stable area close to the landslide, the coordinates of which were measured by D-GNSS.

[12] The surface displacements presented in Figure 4 exhibit an acceleration during summer 2010, before the slope failure. Active creeping in and above the accumulation zone was evidenced by D-GNSS and EDM data (arrows in Figure 4). From July 2009 to May 2010 (green arrows), displacement rate values were lower than 1 m/month. From 21 May to 21 July 2010 (orange arrows), a mean displacement rate of 6 m/month was measured by four targets in the transportation zone. The motion in this zone accelerated from 21 July to 23 August 2010 (purple arrows), when displacements ranging from 17 m up to 21 m were recorded in one month on the same targets. In the meantime, sliding velocities at the head and the secondary scarps were lower than 0.5 m/month.

3.2. Terrestrial Laser Scanning

[13] Terrestrial laser scanning (TLS) was regularly performed from April to September 2010 in order to monitor ground motions over the whole slope. TLS is a remote sensing technique capable of obtaining local images of the earth's 3D topography by acquiring point clouds of the ground position [*Baltsavias*, 1999; *Lichti et al.*, 2002]. TLS involves sending a laser pulse in a known direction and the distance is evaluated by measuring the return time of the pulse reflected by the ground surface. Scanning on a regular grid provides images of several million points. The TLS device was an Optech ILRIS-3D-ER using a laser with a 1500 nm wavelength and with maximum acquisition distance ranging from 800 to 1200 m.

[14] The TLS data acquisition and processing followed these main stages: (1) the point clouds of the upper part of the Pont Bourquin landslide were acquired from the same scanning point of view at different epochs with a mean resolution of 30 mm (average distance between points); (2) two TLS points clouds, from May and July 2010, were selected in order to extract the two months displacements prior to the August event; (3) each points cloud was cleaned, deleting outliers and vegetation masking the ground, using the Pifedit software (InnovMETRIC); (4) the reference point cloud (May 2010) was georeferenced using PolyWorks® v10, ImAlign module, wrapping it on the regional 1 m DEM using the iterative closest point algorithm [*Besl and McKay*, 1992] implemented in PolyWorks®; (5) the second point cloud (July 2010) was aligned and wrapped on the reference cloud with the iterative closest point algorithm, ignoring the unstable area; and (6) the displacements were measured using PolyWorks® v10, ImInspect module. The method computed the horizontal difference between the two surfaces along a north-south axis (i.e., the *y* axis, parallel to the landslide main displacement direction). The error was assumed to be smaller than the alignment error (standard deviation of 35 mm) using the iterative closest point algorithm between the two scans, which was considered small compared to the total displacement.

[15] As shown in Figure 5, TLS surface displacement data, acquired between May and July 2010, can be separated into several distinct areas. On the head scarp, erosion has been recorded, highlighting the occurrence of small earthflow events with a topographic change of less than 0.7 m. In contrast, the middle section of the Pont Bourquin landslide, below the secondary scarp, has been very active and affected by several small translational sliding events shown by positive and negative displacements greater than 1 m in two

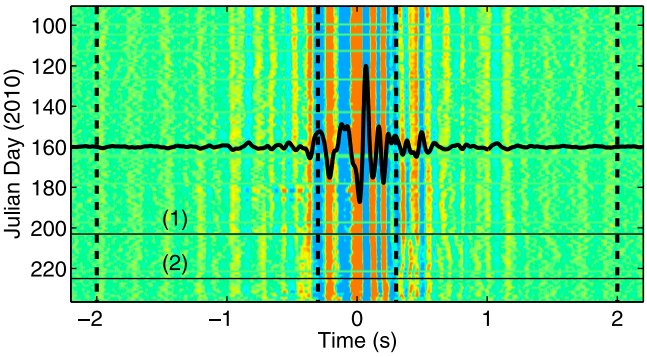

Figure 6. Daily cross correlations of ambient seismic noise recorded by S1 and S2 from day 91 to day 236, in the 4–25 Hz frequency range. Amplitude is normalized each day. The reference trace, averaged over all the correlograms, is displayed by the continuous thick line. Vertical dotted lines mark the time window of the coda used to estimate the relative velocity change dV/V. Early arrivals (between −0.2 s and +0.2 s) are not taken into account in this study. Horizontal lines 1 and 2 mark the days for which a velocity drop is observed (see Figure 7).

months. Large positive motions exceeding 1 m were recorded in the transportation zone (see also Text S1).

4. Ambient Noise Monitoring

4.1. Experimental Procedure and Relative Velocity Change

[16] In order to monitor the change in seismic properties of the material constituting the bulk of the landslide, two seismic sensors S1 and S2 (2 Hz three-component velocimeters) were placed 35 m apart in stable ground on both sides of the landslide (Figures 1, 4, and 5), outside of the active landslide. Moreover, no evidence of recent ground deformations was observed at the two seismometer locations. They were buried at a depth of about 40 cm, to avoid atmospheric thermal effects. They were both connected to the same 24 bit Kephren acquisition station for digitization (at 250 Hz) and data storage. Vertical vibrations were continuously recorded from 1 April to 24 August 2010 and stored in 1 hour long records named $s_1(day,i,t)$ and $s_2(day,i,t)$, respectively, where the subscripts stand for the sensor number, *day* for the date and *i* for the hour.

[17] The records were studied in the 4–25 Hz frequency range, which corresponds to Rayleigh wave penetration depths ranging from a few meters to a few tens of meters, thus sampling the landslide properly. From direct observations during the field experiments, two main sources of ambient noise were identified in this frequency band: the wind in the trees and the traffic along the road at the foot of the landslide. While the noise from both sources may be variable in time, the important feature for monitoring is that their locations are stable [*Hadziioannou et al.*, 2009]. Moreover, although the traffic is not stable in the short term, it statistically stabilizes when averaging over a day, as will be shown below. Although these two sources dominate the seismic noise records, it cannot be excluded that additional distant sources might play a role here, but this issue cannot be studied using a two-sensor experimental setup.

[18] As a first processing step, records were whitened in the 4–25 Hz frequency band. This procedure renormalizes the Fourier transform of s_i at each frequency by its absolute value to ensure that all frequencies in the bandwidth of interest have a similar statistical contribution:

$$\tilde{s}_i(day,i,t) = IFFT\left(\frac{FFT(s_i(day,i,t))}{|FFT(s_i(day,i,t))|}A(\omega)\right), \qquad (2)$$

where $A(\omega)$ is an apodization window in the frequency domain, which shows a smooth transition from 0 (out of the 4–25 Hz range) to 1 (within the 4–25 Hz range).

[19] Then, 24 h cross correlations were calculated and averaged each day, yielding 146 daily correlograms h_{day} for the period of interest:

$$h_{day}(\tau) = \left\langle \int \tilde{s}_1(day,i,t)\tilde{s}_2(day,i,t+\tau)dt \right\rangle_{i=0..23}. \qquad (3)$$

Figure 6 shows the daily cross correlations obtained from Julian day 91 to Julian day 236, along with the reference waveform h_{ref} obtained by averaging all the correlograms. Daily correlations were then filtered at successive center frequencies f_c from 5 Hz to 23 Hz with a 2 Hz bandwidth. For each frequency f_c, correlations are compared to the reference. In the case of a homogeneous velocity change *dV*, all the waveforms constituting the correlograms are shifted in time by a factor *dV/V*. To measure this relative velocity change, the stretching technique [*Sens-Schönfelder and Wegler*, 2006; *Hadziioannou et al.*, 2009] was applied, which consists in testing several possible velocity changes *dV/V* by resampling the correlograms in time $h^{f_c}_{day}(t) \rightarrow h^{f_c}_{day}(t(1 + dv/v))$. The actual relative velocity change *dV/V* at a given date *day* maximizes the correlation coefficient:

$$CC\left(\frac{dV}{V}\right) = \frac{\int h_{day}(t(1+dV/V))h_{ref}(t)dt}{\sqrt{\int h_{day}(t(1+dV/V))^2dt \int h_{ref}(t)^2dt}}. \qquad (4)$$

The asymmetry of the correlograms in the central part [−0.2 s–0.2 s] (Figure 6) is due to the imperfect spatial distribution of noise sources. Signals observed around $\tau = 0$ correspond to waves traveling from the (unknown) sources to the receivers. As these early direct waves (P, S and Rayleigh) are very sensitive to changes in the noise source position, they were removed by considering the portion of the correlograms in the range ([−0.2 s–2 s] and [0.2 s 2 s], delimited by vertical broken lines in Figure 6). This time range begins after the slowest Rayleigh wave between the two sensors and ends when the amplitude of the correlations is low and the waveforms fluctuate too much from one day to another. Consequently, these time windows correspond to coda waves which have sampled the region around and between the seismic sensors [*Pacheco and Snieder*, 2005; *Rossetto et al.*, 2011]. The coda is essentially made up of surface waves [*Larose et al.*, 2006; *Sens-Schönfelder and Wegler*, 2006; *Brenguier et al.*, 2008a, 2008b], i.e., Rayleigh waves for the vertical components used here. The relative phase velocity changes were analyzed for 2 Hz wide frequency bands between 4 and 25 Hz. A significant variation versus time was found in the 10–12 Hz range (Figure 7a). Figure 7a also shows the water table level. Figure 7b displays the plot of the correlation coefficient *CC* between the reference and the current

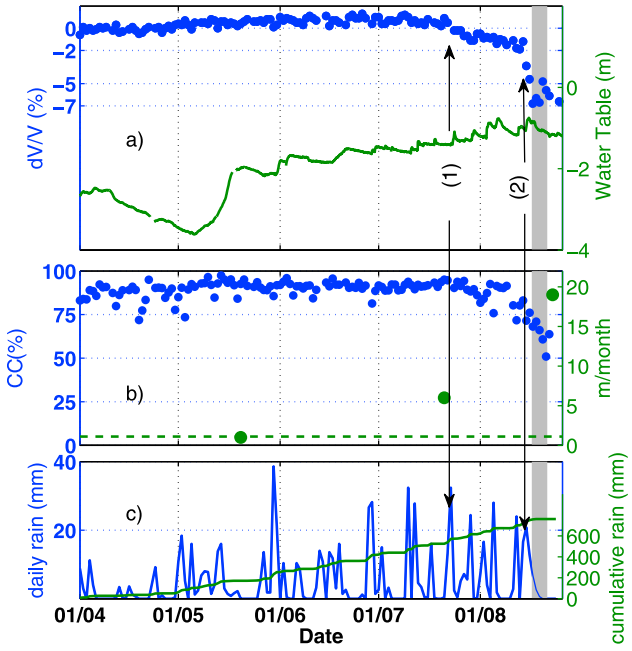

Figure 7. (a) Green represents the water table, and blue represents the relative Rayleigh wave seismic velocity change of the material obtained by comparing daily seismic noise correlograms in the 10–12 Hz frequency range. Vertical line 1: the first velocity reduction starts after rainfall on 23 July and represents a drop of 2% developing over 20 days. Vertical line 2: the major drop starts after rainfall on 14 August, with a total decrease of 7% over the 4 days preceding a major failure of the landslide. The vertical shaded area marks the days of the failure (around 19 August). The correlation coefficient CC, from which the absolute error in estimating dV/V can be derived. This absolute error is 1% for all the data except the last 10 days, where it increases to 2%. (c) Daily (blue) and cumulative (green) precipitation, which cannot alone be used to predict the failure.

correlation (see equation (4)). From this coherence, the absolute error of dV/V can be estimated following *Weaver et al.* [2011]. This error is 1% for all the data except during the last 10 days when it increases to 2%. Figure 7b also gives the average monthly displacement of the landslide computed from the four D-GNSS campaigns. These data show an acceleration of the landslide during summer 2010, but with a limited temporal resolution inherent to this observational technique. Finally, the daily precipitation and the cumulative rainfall are displayed in Figure 7c.

[20] From the beginning of April to the middle of July 2010, the apparent Rayleigh wave velocity was relatively stable: observed velocity fluctuations are smaller than 1%. From mid-May to mid-July, the cumulative rainfall, along with the groundwater level in the piezometer borehole (Figures 7a and 7c), rose linearly with time. Groundwater reacted with a delay of about 20 h to rainfall inputs, suggesting that water infiltration was controlled by soil permeability. On July 24, after a short rainfall event and the corresponding delayed groundwater elevation, the apparent Rayleigh wave velocity (Figure 7a) underwent a gradual decrease of 2% over 20 days. On 15 August, after a series of intense precipitation events and related increases in the water table, the apparent velocity dropped by 7% in only 4 days. While losing its rigidity, the creeping material reached its stability limit and the slope failed, with a composite earthslide-earthflow event. This catastrophic event occurred between 18 and 20 August. As the mud accumulation at the slope toe directly threatened the road, slope reprofiling and drainage works were initiated on 21 August, which led to the seismic devices being dismantled.

4.2. Spectral Analysis of the Relative Velocity Change

[21] Figure 8 displays the Rayleigh wave phase velocity variation evaluated for each frequency band during the

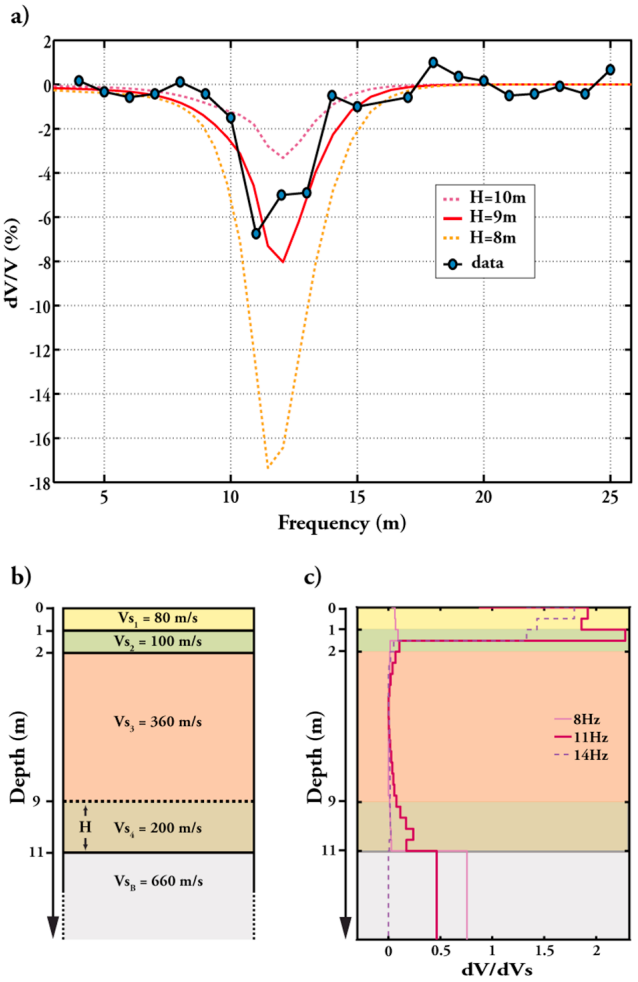

Figure 8. (a) Relative velocity variation dV/V (%) observed in the coda of the correlations for the 5 days preceding the slope failure, for various frequencies (+/−1 Hz around central frequency). The velocity drop is observed mainly in the 10–14 Hz frequency range, corresponding to the lower layer of the sliding material (depth from about 9 to 11 m). Models with different thickness layer (continuous and dotted lines) were tested, and a good fit was obtained with H = 2 m and V_s = 200 m/s in the layer (Figure 8b). (b) V_s model obtained from geophysical prospecting and by fitting the characteristics of the low-velocity layer above bedrock (see section 4.2 for details). (c) Rayleigh wave depth sensitivity kernel computed at the frequencies 8 Hz, 11 Hz, and 14 Hz for the model in Figure 8b.

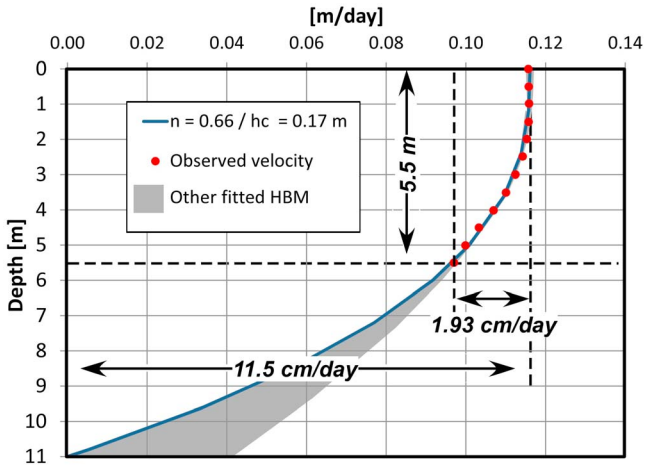

Figure 9. Red dots are observed displacement rates versus depth. Blue line represents velocity profile (corrected for the slope) computed from the Herschel-Bulkley model (HBM) with the fit parameters n = 0.66, h_C = 0.17 m (t_C = 1.4 kPa), and $\mu_n = 1.7 \times 10^{9N\ m-2}\ s^n$. The shaded area shows all the HBMs fitting well the data (the coefficient of determination of the fitted law is r^2 = 0.98). The model giving the greatest velocity at the surface was chosen because it is closer to the observed surface velocities.

5 days before slope failure. It shows that the seismic velocities for frequencies below 10 Hz and above 14 Hz remained unaffected during the course of the experiment and that the velocity drop occurred at a depth related to the sensitivity of Rayleigh waves in the range 10–14 Hz.

[22] In order to define the depth of the change in the sliding material, an analysis of the depth sensitivity of the Rayleigh wave versus frequency is performed similarly to *Rivet et al.* [2011]. An initial numerical model was created from geophysical a priori information and field observations (Figures 2 and 3). From the active seismic profiles, the bedrock depth was fixed at 11 m with V_{sB} = 640 m/s. This bedrock is overlain with a softer layer with a velocity V_{s3} = 360 m/s. Several tests quickly showed that the change at 14 Hz observed in Figure 8a can only be obtained when introducing superficial low V_s layers (V_{s1} = 80 m/s; V_{s2} = 100 m/s) with a total thickness of 2 m. From this model (Figure 8b) the initial dispersion curve of Rayleigh waves (similar to observations before the slope failure) was then computed, using the method proposed by *Dunkin* [1965] and implemented in the geopsy software (http://www.geopsy.org). A series of models with a soft layer (thickness H and V_{s4}) added at the bedrock top was then tested. Figure 8a shows the relative phase velocity differences between the initial and perturbed models, computed for three different thickness values (H = 1, 2 and 3 m) and for a shear wave velocity of V_{s4} = 200 m/s. The best correlation with experimental data was obtained for a thickness H = 2 m (red line). A multitude of realistic models (changing H and V_{s4}) were created to test the uniqueness of this solution and no other simulated model was found consistent with observations. Finally, we computed the Rayleigh wave sensitivity kernels *dV/dVs* as a function of depth for the fundamental mode in order to assess how well the depth localization of the low-velocity layer is constrained. Computations were made for the proposed velocity model at the three frequencies 8 Hz, 11 Hz and 14 Hz (Figure 8c), using the software developed by Herrmann (http://www.eas.slu.edu/People/RBHerrmann), and the sensitivity curves are displayed in Figure 8c. At 8 Hz and 14 Hz, phase velocities are only sensitive to V_s variations in the bedrock and in the shallow layers, respectively. In contrast, the phase velocity at 11 Hz is sensitive to V_s changes both in the shallow layers and, to a less extent, in the two meters above the bedrock interface. However, as no variation was observed on the *dV/V* curve for 14 Hz (Figure 8a), the drop at 11 Hz results from a variation in V_s above the bedrock, corroborating our analysis. The frequency range for which a velocity reduction is observed then corresponds to a V_{s4} decrease from 360 m/s to 200 m/s in a 2 m thick zone located in the lower part of the sliding layer (from 11 to 9 m depth). These results have proved to be robust when varying the characteristics of the soft superficial layers.

4.3. Rheological Analysis of the Inclinometer Data

[23] The depth and intensity of the relative velocity change has been compared with inclinometric data collected in 2009, and with the subsequent rheological considerations derived from them. The 17–21 m surface displacements measured from 21 July to 23 August 2010 can be explained by (1) basal sliding, (2) deformation over a given thickness resulting from a change in rheological properties or (3) both the above factors. Simulating the propagation of the 2007 mudflow using the BING software [*Imran et al.*, 2001] demonstrated that the first hypothesis was not valid [*Jaboyedoff et al.*, 2009]. The only way to explain surface displacements was to introduce a viscoplastic law, like the Herschel-Bulkley model (HBM) [*Coussot*, 1997; *Huang and García*, 1998]. A change in the rheological properties over a certain thickness is also strongly supported by the seismic velocity changes observed in the bulk of the lower part of the sliding material. Here we investigate the most probable rheological model, analyzing the inclinometer data.

[24] In June 2009, about 1 year before the seismic noise experiment, a borehole (I1; 5.5 m deep) was drilled at the top of the Pont Bourquin landslide (see location in Figures 1 and 4). It was equipped with an inclinometer casing. Inclinometer measurements were taken over a short period of time (a few days) after which the high deformation rates destroyed the casing. Since the landslide did not evolve too much from June 2009 to June 2010, the vertical distribution of the deformations in 2010 must be similar to the one obtained in 2009. The velocities were calculated from the inclinometric data. Measurements were projected along the vertical direction assuming an average slope of β = 25°. These data indicate a maximum southward surface displacement of 15.5 cm in 8 days, from 24 June 2009 to 1 July 2009. This motion corresponds to a surface velocity of 1.93 cm/d over a thickness of 5.5 m (Figure 9), with a thin layer in rigid motion overlying a thick layer affected by continuous shearing. The strain rate was found to be negligible at the surface of the profile and accelerates below a depth h_c. This suggests a viscoplastic behavior of the sliding material. Rheological studies of mud have shown that it can be modeled as a non-Newtonian fluid exhibiting a yield

stress and the HBM was found to be appropriate in fitting the rheological data [*Coussot*, 1997]. In the HBM, the velocity profile $u(z\text{-}h_c)$ at a depth $z \geq h_c$ follows the equation

$$u(z) = u_S - \frac{n}{n+1}\left(\frac{\rho g (z-h_c)^{n+1}\sin(\beta)}{\mu_n}\right)^{1/n}, \quad (5)$$

where u_S is the velocity at the surface, n is the exponent of the HBM, h_c is the plug layer (unsheared) thickness, ρ the material density, g the gravity, β the slope angle, μ_n the dynamic viscosity [N m^{-2} s^n], and z is the axis perpendicular to the slope.

[25] The yield stress τ_C is related to h_C by

$$\tau_C = \rho g h_C \sin(\beta). \quad (6)$$

The HBM was fitted by minimizing the absolute difference between theoretical values and raw data. The best fitting curve (Figure 9) was obtained for the following parameters: $\mu_n = 1.7 \times 10^9$ N m^{-2} s^n, $n = 0.66$, $h_c = 0.17$ m and $\tau_C = 1.4$ kPa. The HBM was then used to extrapolate the surface displacement velocity to the base of the sliding material at a depth of 11 m. This depth was deduced from the electrical tomography and the V_s profile. The surface velocity obtained from the HBM is equal to 11.5 cm/d (Figure 9). This surface displacement rate is of the order of magnitude of the observed surface velocity at the center of the landslide (18.2 cm/d) during the period from 20 May to 21 July 2010. The discrepancy between observed and calculated data is interpreted as a slip along a basal surface of the slide. These results indicate that 70% of the displacement rate occurred between 7 m and 11 m depth, and highlight the deformation at the base of the sliding layer, already shown by the relative velocity changes derived from surface waves. The 2010 landslide interpretation is that the gravitational stress locally increased in the accumulation zone and exceeded the yield stress, generating a decrease in the material rigidity, as observed by the ambient noise measurements.

5. Discussion and Conclusions

[26] The Pont Bourquin landslide is a composite active wet earthslide-earthflow composed of clayey material with rock debris, continuously affected by numerous internal and superficial mass movements, as illustrated by the 2007 and 2010 events. From geophysical surveys, the depth of the main slip surface spatially ranges from a few m to about 11 m. Surface displacement monitoring has shown that the mass slides at mean velocities of about one to a few m/month and that a significant velocity increase in and above the accumulation zone was observed in July and August 2010, before slope failure. Due to continuous landslide activity, a bulge of remolded material (observed by Terrestrial Laser Scanning and Electronic Distance Meter) accumulated in the zone where the 2010 failure occurred. From ambient noise measurements and processing, a significant drop (7%) in Rayleigh wave velocity was observed a few days before the event, after an initial gentler decrease (2%). The frequency range (10–14 Hz) for which this drop occurred corresponds to a decrease in shear wave velocity in a 2 m thick layer located between 9 m and 11 m. This significant velocity decrease is interpreted as resulting from the decay in clay mechanical property (rigidity) in the lower part of the layer in motion, precluding the rupture. This is in agreement with a yield stress viscoplastic behavior, for which the material flows once a critical yield stress has been exceeded. For the 2010 event, the gravitational stress was locally increased by the long-term accumulation of the displaced material.

[27] This study has shown that it is possible to detect mechanical behavior changes in the sliding material by monitoring ambient seismic noise, which offers new insights into the rheology of landslides. The observed significant drop in seismic velocity prior to slope failure suggests that time-dependent variation in this parameter could be a valuable precursor. This method could be applied to all clay-rich earthslides, particularly those regularly affected by earthflows and debris flows occurring in the same areas, i.e., at the boundary between the accumulation zone and a lower well-defined narrow track area [*Malet et al.*, 2005; *Picarelli et al.*, 2005]. For large earthslides, small-scale earthflows can be independently triggered all along the different scarps, and a more complex array of receivers would then be required. From a methodological point of view, the present method could be applied where the background seismic noise is excited at frequencies that are relevant to monitor the structure: from the order of 1 Hz for deep and thick edifices (100 m or more) to a few tens of Hz for shallower ones (a few meters depth). Three conditions are requested to apply the method: (1) at least some sources of ambient noise have to remain stable in position during the observation time (river, road, factories, wind or oceanic activity), (2) the subsurface in the area is not affected by other external changes than the landslide itself (large excavation works, mining), and (3) the receivers have a fixed and stable position and orientation.

[28] The method, which has proved to be efficient in a clay-rich landslide, could also be successfully applied in coarser material, including loose sandy soils, provided that a precursor rigidity change can be observed. In large-scale landslide experiments on loose sandy soils, rapid movements were triggered by rising pore water pressure [*Iverson et al.*, 2000]. During the precursory period, the wetting caused soil compaction and a decrease in porosity from 0.52 to 0.49 (6% variation). No V_s measurement was made during this experiment, but we can try to estimate the V_s change resulting from this porosity decrease. *Fawad et al.* [2011] performed V_s measurements during the compaction of sand samples and calibrated an effective law to relate V_s and the porosity for different stresses. Using this law, the porosity decay measured by *Iverson et al.* [2000] is expected to provoke a V_s increase of more than 10%, a value far over the 2% velocity change detected in the Pont Bourquin landslide. These results give hope that the application of ambient seismic noise monitoring could be extended to rapid mass movements in coarse soil. In rocks, ambient noise measurements were recently applied to study the evolution of the natural frequencies of a rock column until its fall [*Lévy et al.*, 2010]. The cross-correlation technique used in the present study could constitute an alternative to the resonance frequency determination for detecting and monitoring medium changes like fracturing in rock slopes. This issue has to be investigated in the future.

[29] **Acknowledgments.** This work was supported by the French ANR project SISCA, the European project "Mountain Risks" (Marie Curie program), and the Department of Isère (France) through the Pôle Grenoblois des Risques Naturels. E.L. acknowledges support from the ERC WHISPER grant. The seismic experiment was operated and maintained by A. Mariscal and L. Darras. The authors would like to thank L. Baron, A. Pedrazzini, A. Loye, M. Choffet, D. Carrea, T. Planes, L. Chaumond, G. Bacques, P. Bottelin, J. Letort, and V. Lebrouc for their participation in the seismic measurements. The authors also thank the editor and three anonymous reviewers for their valuable comments.

References

Angeli, M. G., A. Pasuto, and S. Silvano (2000), A critical review of landslide monitoring experiences, *Eng. Geol. Amsterdam*, *55*, 133–147, doi:10.1016/S0013-7952(99)00122-2.

Badoux, H., J. H. Gabus, and C. H. Mercanton (1990), Les Diablerets, in *Swiss Geological Atlas*, sheet 1285, scale 1:25000, Swiss Fed. Off. for Water and Geol., Wabern, Switzerland.

Baltsavias, E. P. (1999), Airbone laser scanning: Basic relations and formulas, *ISPRS J. Photogramm. Remote Sens.*, *54*, 199–214, doi:10.1016/S0924-2716(99)00015-5.

Besl, P. J., and N. D. McKay (1992), A method for registration of 3-D shapes, *IEEE Trans. Pattern Anal. Mach. Intel.*, *14*(2), 239–256, doi:10.1109/34.121791.

Bièvre, G., U. Kniess, D. Jongmans, E. Pathier, S. Schwartz, C. van Westen, T. Villemin, and V. Zumbo (2011), Paleotopographic control of landslides in lacustrine deposits (Trièves plateau, French western Alps), *Geomorphology*, *125*, 214–224, doi:10.1016/j.geomorph.2010.09.018.

Brenguier, F., N. M. Shapiro, M. Campillo, V. Ferrazzini, Z. Duputel, O. Coutant, and A. Nercessian (2008a), Towards forecasting volcanic eruptions using seismic noise, *Nat. Geosci.*, *1*, 126–130, doi:10.1038/ngeo104.

Brenguier, F., M. Campillo, C. Hadziioannou, N. M. Shapiro, R. M. Nadeau, and E. Larose (2008b), Postseismic relaxation along the San Andreas fault at Parkfield from continuous seismological observations, *Science*, *321*, 1478–1481, doi:10.1126/science.1160943.

Coe, J. A., W. L. Ellis, J. W. Godt, W. Z. Savage, J. E. Savage, J. A. Michael, J. D. Kibler, P. S. Powers, D. J. Lidke, and S. Debray (2003), Seasonal movement of the Slumgullion landslide determined from Global Positioning System surveys and field instrumentation, July 1998–March 2002, *Eng. Geol. Amsterdam*, *68*, 67–101, doi:10.1016/S0013-7952(02)00199-0.

Coussot, P. (1997), *Mudflow Rheology and Dynamics*, *IAHR Monogr. Ser.*, 272 pp., Taylor and Francis, London.

Crawford, C. B. (1968), Quick clays of eastern Canada, *Eng. Geol. Amsterdam*, *2*, 239–265, doi:10.1016/0013-7952(68)90002-1.

Crosta, G. B., and P. Frattini (2008), Rainfall-induced landslides and debris flows, *Hydrol. Processes*, *22*, 473–477, doi:10.1002/hyp.6885.

Cruden, D. M., and D. J. Varnes (1996), Landslide types and processes, in *Landslides, Investigation and Mitigation*, edited by A. K. Turner and R. L. Schuster, *Spec. Rep.—Natl. Res. Counc., Transp. Res. Board*, *247*, 36–75.

Dahlin, T., and B. Zhou (2004), A numerical comparison of 2D resistivity imaging with 10 electrode arrays, *Geophys. Prospect.*, *52*, 379–398, doi:10.1111/j.1365-2478.2004.00423.x.

Dunkin, J. W. (1965), Computation of modal solutions in layered, elastic media at high frequencies, *Bull. Seismol. Soc. Am.*, *55*, 335–358.

Eilertsen, R. S., L. Hansen, T. H. Bargel, and I.-L. Solberg (2008), Clay slides in the Målselv valley, northern Norway: Characteristics, occurrence, and triggering mechanisms, *Geomorphology*, *93*, 548–562, doi:10.1016/j.geomorph.2007.03.013.

Fawad, M., N. H. Mondol, J. Jahren, and K. Bjørlykke (2011), Mechanical compaction and ultrasonic velocity of sands with different texture and mineralogical composition, *Geophys. Prospect.*, *59*, 697–720, doi:10.1111/j.1365-2478.2011.00951.x.

Gili, J. A., J. Corominas, and J. Rius (2000), Using Global Positioning System techniques in landslide monitoring, *Eng. Geol. Amsterdam*, *55*, 167–192, doi:10.1016/S0013-7952(99)00127-1.

Hadziioannou, C., E. Larose, O. Coutant, P. Roux, and M. Campillo (2009), Stability of monitoring weak changes in multiply scattering media with ambient noise correlation: Laboratory experiments, *J. Acoust. Soc. Am.*, *125*, 3688–3695, doi:10.1121/1.3125345.

Huang, X., and M. H. García (1998), A Herschel-Bulkley model for mud flows down a slope, *J. Fluid Mech.*, *374*, 305–333, doi:10.1017/S0022112098002845.

Imran, J., P. Harff, and G. Parker (2001), A numerical model of submarine debris flow with graphical user interface, *Comput. Geosci.*, *27*, 717–729, doi:10.1016/S0098-3004(00)00124-2.

Iverson, R. M., M. E. Reid, and R. G. LaHusen (1997), Debris flow mobilization from landslides, *Annu. Rev. Earth Planet. Sci.*, *25*, 85–138, doi:10.1146/annurev.earth.25.1.85.

Iverson, R. M., M. E. Reid, N. R. Iverson, R. G. LaHusen, M. Logan, J. Mann, and D. L. Brien (2000), Acute sensitivity of landslide to initial soil porosity, *Science*, *290*, 513–516, doi:10.1126/science.290.5491.513.

Jaboyedoff, M., A. Pedrazzini, A. Loye, T. Opikofer, I. Güell, M. Pons, and J. Locat (2009), Earth flow in a complex geological environment: The example of Pont Bourquin, Les Diablerets (Western Switzerland), in *Landslide Processes, From Geomorphologic Mapping to Dynamic Modelling*, edited by J. P. Malet, A. Remaître, and T. Bogaard, pp. 131–137, CERG Ed., Strasbourg, France.

Keefer, D. K., R. C. Wilson, R. K. Mark, E. E. Brabb, W. M. Brown, S. D. Ellen, E. L. Harp, G. F. Wieczorek, C. S. Alger, and R. S. Zatkin (1987), Real-time landslide warning during heavy rainfall, *Science*, *238*, 921–925, doi:10.1126/science.238.4829.921.

Lacoss, R. T., E. J. Kelly, and M. N. Toksoz (1969), Estimation of seismic noise structure using arrays, *Geophysics*, *34*, 21–38, doi:10.1190/1.1439995.

Larose, E., L. Margerin, A. Derode, B. van Tiggelen, M. Campillo, N. Shapiro, A. Paul, L. Stehly, and M. Tanter (2006), Correlation of random wave fields: An interdisciplinary review, *Geophysics*, *71*, SI11, doi:10.1190/1.2213356.

Lee, K. T., and J. Y. Ho (2009), Prediction of landslide occurrence based on slope-instability analysis and hydrological model simulation, *J. Hydrol.*, *375*, 489–497, doi:10.1016/j.jhydrol.2009.06.053.

Lévy, C., L. Baillet, D. Jongmans, P. Mourot, and D. Hantz (2010), Dynamic response of the Chamousset rock column (western Alps, France), *J. Geophys. Res.*, *115*, F04043, doi:10.1029/2009JF001606.

Lichti, D. D., S. J. Gordon, and M. P. Stewart (2002), Ground-based laser scanners: Operation, systems and applications, *Geomatica*, *56*, 21–33.

Loke, M. H. (1998), RES2DINV, Rapid 2D resistivity and IP inversion using the least-squares method, user manual, 66 pp., Adv. Geosci., Inc., Austin, Tex.

Malet, J. P., D. Laigle, A. Remaître, and O. Maquaire (2005), Triggering conditions of debris-flows associated to complex earthflows, *Geomorphology*, *66*, 215–235, doi:10.1016/j.geomorph.2004.09.014.

Pacheco, C., and R. Snieder (2005), Time-lapse travel time change of multiply scattered acoustic waves, *J. Acoust. Soc. Am.*, *118*, 1300–1310, doi:10.1121/1.2000827.

Petley, D. N., F. Mantovani, M. H. Bulmer, and A. Zannoni (2005), The use of surface monitoring data for the interpretation of landslide movement patterns, *Geomorphology*, *66*, 133–147, doi:10.1016/j.geomorph.2004.09.011.

Picarelli, L., L. Urciuoli, G. Ramondini, and L. Comegna (2005), Main features of mudslides in tectonised highly fissured clay shales, *Landslides*, *2*(1), 15–30, doi:10.1007/s10346-004-0040-2.

Renalier, F., G. Bièvre, D. Jongmans, M. Campillo, and P.-Y. Bard (2010), Clayey landslide investigations using active and passive V_s measurements, in *Advances in Near-Surface Seismology and Ground-Penetrating Radar*, *Geophys. Dev. Ser.*, vol. 15, edited by R. D. Miller, J. H. Bradford, and K. Holliger, chap. 24, pp. 397–414, Soc. of Explor. Geophys., Tulsa, Okla.

Reynolds, J. M. (1997), *An Introduction to Applied and Environmental Geophysics*, 796 pp., John Wiley, Chichester, U. K.

Rivet, D., M. Campillo, N. M. Shapiro, V. Cruz-Atienza, M. Radiguet, N. Cotte, and V. Kostoglodov (2011), Seismic evidence of nonlinear crustal deformation during a large slow slip event in Mexico, *Geophys. Res. Lett.*, *38*, L08308, doi:10.1029/2011GL047151.

Rossetto, V., L. Margerin, T. Planès, and E. Larose (2011), Locating a weak change using diffuse waves: Theoretical approach and inversion procedure, *J. Appl. Phys.*, *109*, 034903, doi:10.1063/1.3544503.

Sens-Schönfelder, C., and U. Wegler (2006), Passive image interferometry and seasonal variations of seismic velocities at Merapi Volcano, Indonesia, *Geophys. Res. Lett.*, *33*, L21302, doi:10.1029/2006GL027797.

Shapiro, N. M., and M. Campillo (2004), Emergence of broadband Rayleigh waves from correlations of the ambient seismic noise, *Geophys. Res. Lett.*, *31*, L07614, doi:10.1029/2004GL019491.

Shapiro, N. M., M. Campillo, L. Stehly, and M. H. Ritzwoller (2005), High-resolution surface-wave tomography from ambient seismic noise, *Science*, *307*, 1615–1618, doi:10.1126/science.1108339.

U.S. Army Corps of Engineers (2003), NAVSTAR Global Positioning System surveying, *Eng. Manual EM 1110-1-1003*, 469 pp., U.S. Dept. of the Army, Washington, D. C.

U.S. Army Corps of Engineers (2007), Control and topographic surveying, *Eng. Manual EM 1110-1-1005*, 498 pp., U.S. Dept. of the Army, Washington, D. C.

van Asch, T. W. J., T. A. Van Beek, and L. P. H. Bogaard (2007), Problems in predicting the mobility of slow-moving landslides, *Eng. Geol. Amsterdam*, *91*, 46–55, doi:10.1016/j.enggeo.2006.12.012.

Wathelet, M. (2008), An improved neighborhood algorithm: Parameter conditions and dynamic scaling, *Geophys. Res. Lett.*, *35*, L09301, doi:10.1029/2008GL033256.

Weaver, R. L., and O. I. Lobkis (2001), Ultrasonics without a source: Thermal fluctuation correlations at MHz frequencies, *Phys. Rev. Lett.*, *87*, 134301, doi:10.1103/PhysRevLett.87.134301.

Weaver, R. L., C. Hadziioannou, E. Larose, and M. Campillo (2011), On the precision of noise correlation interferometry, *Geophys. J. Int.*, *185*, 1384–1392, doi:10.1111/j.1365-246X.2011.05015.x.

C. Brönnimann, GEOLEP, EPFL, Station 18, CH-1015 Lausanne, Switzerland.

M. Jaboyedoff and C. Michoud, IGAR, University of Lausanne, Amphipôle 338, CH-1015 Lausanne, Switzerland.

D. Jongmans, E. Larose, and G. Mainsant, ISTerre, CNRS, Université de Grenoble 1, BP 53, F-38041 Grenoble CEDEX 9, France. (eric.larose@ujf-grenoble.fr)